Equipartitioning and Diffusion in Scattering Media as Local Processes: A Numerical Study Using the Radiative Transfer Equations

Manuel Jaimes & Roel Snieder

Center for Wave Phenomena and Dept. of Geophysics, Colorado School of Mines, Golden CO 80401
email mjaimescaballero@mines.edu

ABSTRACT

We study the transition from ballistic to diffusive wave propagation in scattering media using the radiative transfer equations. To solve these equations we first transform them into integral equations for the specific intensities, and then construct a time stepping algorithm with which we evolve the specific intensities numerically in time. We handle the advection of energy analytically to avoid numerical dispersion. With this algorithm we are able to model various initial conditions for the intensity field, non-isotropic scattering, and non-uniform scatterer density. We test this algorithm for an isotropic initial condition, isotropic scattering and uniform scattering density, and find good agreement with analytical solutions. We use this algorithm to numerically investigate the transition from ballistic to diffusive wave propagation over space and time, for two different initial conditions. The first one corresponds to an isotropic Gaussian distribution and the second one to a plane wave segment. We find that equipartitioning and diffusion must be treated as local rather than global concepts. We also show numerically that an energy field which is nearly equipartitioned is not necessarily diffuse. We provide a discussion about the implications that equipartitioning, as a local process, has for Green's functions reconstructions.

Key words: Multiple scattering, Equipartitioning, Diffusion

1 INTRODUCTION

As waves propagate through a scattering medium they lose (or gain) energy due to scattering to (or from) other directions. In the absence of anelastic attenuation, this phenomenon obeys energy conservation, which one may mathematically describe using the radiative transfer equations (RTE). The RTE consist of a coupled system of integro-differential equations where one solves for the wave intensity as a function of space, time and angular direction, assuming one knows the scattering mean free path l, the angular dependence of scattering, and the speed of energy propagation v. Due to its usefulness RTE has been employed in several scientific fields. In astrophysics RTE has been used to analyze radiation transport across cosmic dust in a wide range of astrophysical objects (Steinacker et al., 2002; Narayanan et al., 2021; Wolf, 2003); in atmospheric sciences researchers use RTE to model solar radiation across clouds to better understand the evolution of sea surface temperatures (Evans and Stephens, 1995; Aumann et al., 2018; Manners et al., 2009); in optics RTE has been used to develop novel optical tomographic imaging algorithms which allow diagnosis and treatment of biological tissues (Klose et al., 2002; Abdoulaev, 2003; Ren et al., 2004; Yodh and Chance, 1995); in acoustics RTE has been used for modeling the interaction of acoustic waves with the ocean bottom (Quijano and Zurk, 2009), modeling of forest acoustics (Ostashev et al., 2017), and modeling of acoustical diffractions by obstacles (Reboul et al., 2005); in geophysics RTE has been used to study infrared radiation across volcanic ash clouds (Prata, 1989; Francis et al., 2012; Lee et al., 2014), modeling of heat transfer in the mantle (Hofmeister, 2005), and computation of scattering kernels in coda wave interferometry (Margerin et al., 2016; Duran et al., 2020; Dinther et al., 2021; Obermann et al., 2016).

Despite its usefulness in describing energy transport, RTE is complicated and numerically demanding due to its dependence on not only space and time, but also on the directions of wave propagation. In 2 dimensions the radiative transfer solution depends

on 4 variables (time, two space variables, and one angle). In 3 dimensions it depends on 6 variables (time, three space variables, and two angles). Numerical techniques that have been used to solve the RTE include

- the discontinuous Galerkin finite element method, which has a high order accuracy in space and time but requires one to add numerical viscosity in order to avoid nonphysical oscillations in the numerical solution and is computationally expensive (Clarke et al., 2019; Han et al., 2010).
- Markov Chain Monte Carlo techniques, which are quite accurate and applicable to complicated media but are computationally expensive and rely on using enough phonons to sample the intensity field as a function of space, time, and propagation directions (Iwabuchi, 2006; Xu et al., 2011; Camps and Baes, 2018; Noebauer and Sim, 2019; Przybilla and Korn, 2008; Yoshimoto, 2000).
- Finite Difference techniques, which suffer from numerical dispersion in space and time due to the discretization of spatial and temporal derivatives and may produce negative intensities which are nonphysical (Klose and Hielscher, 1999).
- and Wave Equation modeling, whereby one exploits the connection between the acoustic (or elastic) wave equation and the scalar (or elastic) RTE (Przybilla et al., 2006; Kanu and Snieder, 2015; Snieder et al., 2019; Duran et al., 2020). One solves the wave equation for several realization of a medium and computes a statistical average of the intensity field to suppress statistical fluctuations of the intensity field. However, the wave field must be averaged over enough realizations of the medium and one must locally decompose the calculated wave field into different propagation directions to properly account for the directionality of the wave energy transport.

In addition to these numerical techniques there have been analytical approximations to RTE such as assuming diffusive wave propagation which is only valid at times much larger than the transport mean free time (Rossetto et al., 2011; Planès et al., 2014); assuming a point-like, isotropic, impulsive source of intensity in a statistically homogeneous medium (Margerin et al., 2016); expanding the intensity and scattering function into a finite sum of Legendre polynomial and then solving a finite system of equations for the unknown coefficients appearing in a truncated expansion (Roberge, 1983); decomposing the specific intensities into a sum of partial intensities and then solving the RTE for each partial intensity assuming angle-independent scattering (Paasschens, 1997); assuming a steady-state intensity field (Fan et al., 2019; Le Hardy et al., 2016); or assuming azimuthal symmetry (Baes and Dejonghe, 2001; de Abreu, 2004). In search of an efficient and accurate numerical method that overcomes some of the limitations mentioned above we propose a novel numerical scheme to compute the numerical intensities which solve the scalar RTE. Our approach is based on transforming the RTE into an integral equation for the specific intensities and then solving this integral equation as a time-stepping algorithm. Contrary to standard finite difference (FD) or discontinuous Galerkin finite element (DGFE) methods we handle the advection of energy analytically. This means that our numerical procedure for computing the wave energy transport does not introduce the numerical dispersion appearing in such numerical schemes. Further, since the time discretization depends on the transport mean free time, instead of the frequency of the waves, the space and time discretization in the numerical modeling of the radiative transfer equation can be much coarser than it is for wave field modeling.

This paper is organized as follows: In section 2 we discuss the scalar RTE and derive a localized time-stepping algorithm. In section 3 we show numerical simulations for isotropic scattering and compare the computed intensities to exact solutions. We also show how our algorithm handles arbitrary source distributions and angle-dependent scattering and discuss the transition from ballistic to diffusive wave propagation. To quantify this transition we introduce the equipartitioning index, a quantity which ranges from 0 (full equipartitioning) to 1 (uni-directional wave propagation), and emphasize that the transition from ballistic to diffuse waves occurs locally rather than globally. We also show numerically that when an intensity field is nearly equipartitioned, it is not necessarily diffusive, since an additional condition must be satisfied (van Rossum and Nieuwenhuizen, 1999). We conclude section 3 with numerical simulations for a medium with non-uniform scattering properties. In section 4 we discuss the implications that local equipartitioning has for the reconstruction of Green's functions using noise fields. Typically, it is assumed that the field fluctuations with which the Green's functions are to be retrieved have no preferred propagation direction, which is not always the case. In section 5 we discuss the algortihm that we develop, equiparitioning as a local process, the implications that this has for Green's function retrieval, and that almost equipartioning does not necessarily imply that the energy propagation is diffusive.

2 THEORY

2.1 Description of the Scalar Radiative Transfer Equations

The radiative transfer equations (RTE) are a system of coupled integro-differential equations which describe the distribution of energy in a scattering medium as a function of space, time, and direction $\hat{\mathbf{n}}$ of wave propagation (Chandrasekhar, 1960; Turner and Weaver, 1994; Ryzhik et al., 1996). For late times, when the wave propagation is almost independent of direction, and is nearly stationary in time, the equation of radiative transfer leads to diffusive wave transport (van Rossum and Nieuwenhuizen,

1999). The radiative transfer equations follow from the ladder approximation to the Bethe-Salpeter equation (van Rossum and Nieuwenhuizen, 1999) and accurately describe wave transport at both early and late times, as well as the transition from ballistic wave propagation to weak scattering to strong multiple scattering (Paasschens, 1997). In the derivation of the radiative transfer equations one assumes that scattered waves have uncorrelated random phases, resulting in the description of scattering processes in terms of average intensities rather than in terms of stress or material displacement (Turner and Weaver, 1994). To derive the radiative transfer equations one may either make use of energy balance in an infinitesimal volume containing scatterers, or directly derive these equations from the wave equations by estimating the ensemble average of the covariance of the Green's function in a random medium (Turner and Weaver, 1994). For a thorough description of the radiative transfer (transport) equations in random media we refer the reader to Ryzhik et al. (1996).

Assuming a uniform speed of transport and ignoring intrinsic attenuation the scalar radiative transfer equation in 2 dimensions for an intensity field reads (Wu, 1985)

$$\frac{\partial I(\mathbf{r},\hat{\mathbf{n}},t)}{\partial t} + v\hat{\mathbf{n}}\cdot\nabla I(\mathbf{r},\hat{\mathbf{n}},t) = -\frac{1}{\tau_s}I(\mathbf{r},\hat{\mathbf{n}},t) + \frac{1}{\tau_s}\oint f(\hat{\mathbf{n}},\hat{\mathbf{n}}')I(\mathbf{r},\hat{\mathbf{n}}',t)d^2\hat{\mathbf{n}}', \tag{1}$$

where the scattering function $f(\hat{\mathbf{n}},\hat{\mathbf{n}}')$ is assumed to be independent of frequency, which holds for band-limited wavefields. In equation 1 the variable $I(\mathbf{r},\hat{\mathbf{n}},t)$ is the intensity of waves at a location $\mathbf{r}$ and time t propagating in the direction $\hat{\mathbf{n}}$. In the literature of radiative transfer the variable $I(\mathbf{r},\hat{\mathbf{n}},t)$ is referred to as the *specific intensity* (Chandrasekhar, 1960). The advection of the energy, propagating with a wave velocity v, is described by the term $v\hat{\mathbf{n}}\cdot\nabla I(\mathbf{r},\hat{\mathbf{n}},t)$. The parameter τ_s is the scattering mean free time which describes the average time between scattering events. The term $-I(\mathbf{r},\hat{\mathbf{n}},t)/\tau_s$ accounts for the energy that is lost to other directions in the scattering process. The term $\oint f(\hat{\mathbf{n}},\hat{\mathbf{n}}')I(\mathbf{r},\hat{\mathbf{n}}',t)d^2\hat{\mathbf{n}}'/\tau_s$ describes the gain due to energy scattered from other directions. The scattering function $f(\hat{\mathbf{n}},\hat{\mathbf{n}}')$ relates the incident intensity to scattered intensity. This function is normalized, assuming that there is no absorption (van Rossum and Nieuwenhuizen, 1999), such that

$$\oint f(\hat{\mathbf{n}},\hat{\mathbf{n}}')d^2\hat{\mathbf{n}}' = 1. \tag{2}$$

This normalization follows by analyzing eqn. 1 for a homogeneous and time-independent intensity.

2.2 Formulation of the Numerical Algorithm

We solve the 2-D scalar RTE

$$\partial_t I(\mathbf{r},\hat{\mathbf{n}},t) + v\hat{\mathbf{n}}\cdot\nabla I(\mathbf{r},\hat{\mathbf{n}},t) = -I(\mathbf{r},\hat{\mathbf{n}},t)/\tau_s + \oint f(\hat{\mathbf{n}},\hat{\mathbf{n}}')I(\mathbf{r},\hat{\mathbf{n}}',t)d^2\hat{\mathbf{n}}'/\tau_s, \text{for } t > t_0 \tag{3}$$

subject to the initial condition $I_0(\mathbf{r},\hat{\mathbf{n}})$ at an initial time t_0

$$I(\mathbf{r},\hat{\mathbf{n}},t=t_0) = I_0(\mathbf{r},\hat{\mathbf{n}}). \tag{4}$$

In eqn. 3 $\hat{n} = (\cos\theta, \sin\theta)$ indicates the direction of propagation, with θ the counter-clockwise angle relative to the horizontal direction (x-axis). We assume that the computational boundaries are far enough from the source such that the intensities can be assumed to vanish at the boundary.

We transform the initial value problem in equation 3 into an integral equation for the specific intensities (Paasschens, 1997)

$$\begin{aligned} I(x,y,\hat{\mathbf{n}},t) &= I(x - v(t-t_0)\cos(\theta), y - v(t-t_0)\sin(\theta), \hat{\mathbf{n}}, t_0)e^{-(t-t_0)/\tau_s} \\ &+ \frac{1}{\tau_s}\int_{t_0}^{t}\oint f(\hat{\mathbf{n}},\hat{\mathbf{n}}')I(x - v(t-t')\cos(\theta), y - v(t-t')\sin(\theta), \hat{\mathbf{n}}', t')e^{-(t-t')/\tau_s}d^2\hat{\mathbf{n}}'dt'. \end{aligned} \tag{5}$$

Paasschens (1997) analytically solves for the specific intensities in equation 5 for a medium with isotropic scattering and constant scattering properties assuming that the initial condition for the specific intensity is isotropic. To do this, he decomposes the specific intensities into a sum of partial intensities, where each partial intensity signifies a number of scattering events (i.e., direct propagation, single scattering, double scattering, and so on). We show in the appendix that equation 5 solves the radiative transfer equations 3 for the arbitrary initial condition 4 and angle-dependent scattering. In this paper we use equation 5 to integrate the specific intensities numerically in time. This approach allows us to use non-isotropic initial conditions and non-isotropic scattering radiation patterns.

In expression 5 the first term in the right hand side corresponds to the incident intensity which propagates and decays over time due to scattering losses to other directions. The second term corresponds to the scattered intensity which accounts for the energy gain due to scattering from all possible propagation directions. To develop an iterative algorithm which depends only on the current

time t and the previous time step $t-\Delta t$ we replace t_0 by $t-\Delta t$ to obtain

$$I(x,y,\hat{\mathbf{n}},t) = I(x-v\Delta t\cos(\theta), y-v\sin(\theta), \hat{\mathbf{n}}, t-\Delta t)e^{-\Delta t/\tau_s}$$
$$+\frac{1}{\tau_s}\int_{t-\Delta t}^{t}\oint f(\hat{\mathbf{n}},\hat{\mathbf{n}}')I(x-v(t-t')\cos(\theta), y-v(t-t')\sin(\theta),\hat{\mathbf{n}}',t')e^{-(t-t')/\tau_s}d^2\hat{\mathbf{n}}'dt'. \quad (6)$$

The contribution of the incident intensity at time $t-\Delta t$ in equation 5 now becomes the first term in equation 6. The second term in equation 6 corresponds to the scattered contributions at current and previous times. Through this iterative algorithm we compute the advection and scattering of energy locally. We proceed by applying the discrete ordinate method (Chandrasekhar, 1960) whereby one divides the angular integral into N equal segments. In two dimensions this method corresponds to setting $d^2\hat{\mathbf{n}} \to d\theta$ and then setting $d\theta = 2\pi/N$ in the angular integration

$$I(x,y,\hat{\mathbf{n}},t) = I(x-v\Delta t\cos(\theta), y-v\Delta t\sin(\theta), \hat{\mathbf{n}}, t-\Delta t)e^{-\Delta t/\tau_s}$$
$$+\frac{1}{\tau_s}\int_{t-\Delta t}^{t}\sum_{\mathbf{n}'}\frac{2\pi}{N}f(\hat{\mathbf{n}},\hat{\mathbf{n}}')I(x-v(t-t')\cos(\theta), y-v(t-t')\sin(\theta),\hat{\mathbf{n}}',t')e^{-(t-t')/\tau_s}dt'. \quad (7)$$

We then discretize the remaining time integral using the two-point trapezoidal quadrature rule by which we obtain

$$I(x,y,\hat{\mathbf{n}},t) = I(x-v\Delta t\cos(\theta), y-v\Delta t\sin(\theta), \hat{\mathbf{n}}, t-\Delta t)e^{-\Delta t/\tau_s}$$
$$+\frac{1}{\tau_s}\sum_{\hat{\mathbf{n}}'}\frac{\pi}{N}f(\hat{\mathbf{n}},\hat{\mathbf{n}}')I(x-v\Delta t\cos(\theta), y-v\Delta t\sin(\theta),\hat{\mathbf{n}}',t-\Delta t)e^{-\Delta t/\tau_s}\Delta t$$
$$+\frac{1}{\tau_s}\sum_{\hat{\mathbf{n}}'}\frac{\pi}{N}f(\hat{\mathbf{n}},\hat{\mathbf{n}}')I(x,y,\hat{\mathbf{n}}',t)\Delta t. \quad (8)$$

Lastly, we arrange eqn. 8 to obtain

$$I(x,y,\hat{\mathbf{n}},t) - \frac{1}{\tau_s}\sum_{\hat{\mathbf{n}}'}\frac{\pi}{N}f(\hat{\mathbf{n}},\hat{\mathbf{n}}')I(x,y,\hat{\mathbf{n}}',t)\Delta t =$$
$$I(x-v\Delta t\cos(\theta), y-v\Delta t\sin(\theta), \hat{\mathbf{n}}, t-\Delta t)e^{-\Delta t/\tau_s} +$$
$$\frac{1}{\tau_s}\sum_{\hat{\mathbf{n}}'}\frac{\pi}{N}f(\hat{\mathbf{n}},\hat{\mathbf{n}}')I(x-v\Delta t\cos(\theta), y-v\Delta t\sin(\theta),\hat{\mathbf{n}}',t-\Delta t)e^{-\Delta t/\tau_s}\Delta t, \quad (9)$$

where the right-hand side is a known quantity since it only depends on previous time $t-\Delta t$.

Eqn. 9 consists of a system of N equations, with N variables (the intensities at every discretization angle). For an arbitrary number of N directions we write

$$\mathbf{A}\vec{\mathbf{I}} = \vec{\mathbf{S}}. \quad (10)$$

The entries of the vector on the right-hand side of eqn. 10 correspond to the right-hand side of eqn. 9. For a given direction $\hat{\mathbf{n}}_i$ we write

$$S(x,y,\hat{\mathbf{n}}_i,t-\Delta t) = I(x-v\Delta t\cos\theta, y-v\Delta t\sin\theta, \hat{\mathbf{n}}_i, t-\Delta t)e^{-\Delta t/\tau_s}$$
$$+\frac{1}{\tau_s}\sum_{\hat{\mathbf{n}}'}\frac{\pi}{N}f(\hat{\mathbf{n}}_i,\hat{\mathbf{n}}')I(x-v\Delta t\cos\theta, y-v\Delta t\sin\theta,\hat{\mathbf{n}}',t-\Delta t)e^{-\Delta t/\tau_s}\Delta t. \quad (11)$$

The $N\times N$ matrix on the left-hand side of eqn. 10 has entries $A_{ij} = \delta_{ij} - \frac{\pi\Delta t}{N\tau_s}f(\hat{\mathbf{n}}_i,\hat{\mathbf{n}}_j)$. The indices are introduced to emphasize that the scattering function $f(\hat{\mathbf{n}}_i,\hat{\mathbf{n}}_j)$ depends on the incident and scattering angles. This matrix multiplies the intensity vector $\vec{\mathbf{I}}$ that we solve for. The right hand-side of eqn. 10 corresponds to a source term with which we evolve the numerical solution, and depends on the intensities at the previous time, given by eqn. 11.

2.3 Choice of Scattering Function and the Transport Mean Free Time

We use the Henyey-Greenstein (HG) scattering function in 2D to describe a medium with angle-dependent scattering (Margerin et al., 2016).

$$f(\hat{\mathbf{n}},\hat{\mathbf{n}}') = \frac{1}{2\pi}\frac{1-g^2}{(1+g^2-2g(\hat{\mathbf{n}}\cdot\hat{\mathbf{n}}'))}. \quad (12)$$

The variable g describes the level of angle-dependent scattering and it ranges from predominantly backward scattering ($g=-1$) to isotropic scattering ($g=0$) to predominantly forward scattering ($g=1$). For practical purposes one considers the range

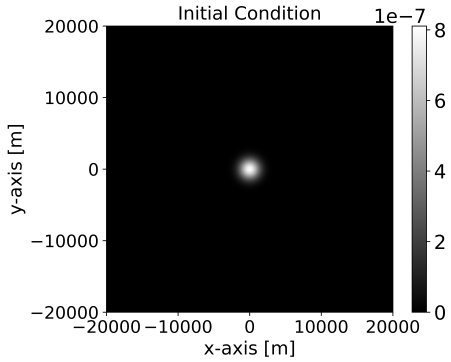

Figure 1. Total intensity at $t = 0$. This initial condition is normalized such that the total energy equals unity.

$-1 < g < 1$ to avoid the singularities for $g = \pm 1$ when $(\hat{\mathbf{n}} \cdot \hat{\mathbf{n}}') = \pm 1$. When scattering depends on angle the time scale at which the scattering events occur is referred to as the transport mean free time τ^*, and it is related to the scattering mean free τ_s time by $\tau^* = \tau_s/(1-g)$ (van Rossum and Nieuwenhuizen, 1999). This relationship implies that if scattering is predominantly in the forward direction $\tau^* > \tau_s$, whereas when scattering is predominantly in the backward direction $\tau^* < \tau_s$.

We normalize the scattering function using a discretized version of eqn 2

$$\sum_{\hat{\mathbf{n}}'} \frac{1}{CN} \frac{1-g^2}{(1+g^2-2g(\hat{\mathbf{n}} \cdot \hat{\mathbf{n}}'))} = 1, \tag{13}$$

where the discrete sum is over N angles. C thus corresponds to a constant

$$C = \sum_{\hat{\mathbf{n}}'} \frac{1}{N} \frac{1-g^2}{(1+g^2-2g(\hat{\mathbf{n}} \cdot \hat{\mathbf{n}}'))}, \tag{14}$$

which we introduce to satisfy the unity of the normalization condition 2 for the discretized scattering function. When $g = 0$ the constant $C = 1$, and when $g \neq 0$ the value of the constant $C \to 1$ as $N \to \infty$.

3 NUMERICAL SIMULATIONS

In the first example the initial condition for the intensity at $t_0 = 0$ consists of a 2-D Gaussian placed at the middle of the computational domain with a full width at half maximum of ≈ 2350 m, where at every point in space energy is emitted equally in all directions. Fig. 1 shows this initial condition as well as the spatial coordinates of the computational domain. Both coordinates range from -20000 m to 20000 m, with a grid spacing $\Delta x = \Delta y = 200$ m. We use a constant propagation velocity $v = 1000$ m/s and scattering mean free time $\tau_s = 5$ s. We integrate the intensities from $t = 0$ to 20 s with Δt = 0.2 s, with the choice of temporal discretization small enough ($\Delta t \ll \tau_s$) to capture the scattering interactions. We use $N = 32$ directions of propagation, equally spaced in the range $[0, 2\pi)$. To compute the advection terms which do not lie on grid points we perform linear interpolation, which is a sufficiently good approximation provided that the initial condition is smooth. In our numerical experiments we find that ten sample points for the full-width at half-maximum are enough to avoid interpolation artifacts. At the boundary we set the intensities equal to zero, which does not affect the accuracy of our results for the distances and propagation times that we investigate.

3.1 Comparison of numerical and exact solutions for isotropic scattering

We compare the analytical and numerical specific intensities as derived by Paasschens (1997), rather than the total intensities, for a medium with isotropic scattering. This comparison allows us to assess the accuracy of our algorithm in retrieving the individual specific intensities since the total intensity may average out discrepancies between the numerical and analytical solutions of the specific intensities.

Figure 2 shows the comparison between analytical and numerical solutions for the specific intensities at different angular directions at a distance of 5000 m from the Gaussian peak in fig. 1. The direction aligned with the radial direction shows the largest amplitude, and the magnitude of the specific intensity decreases with increasing angle θ relative to the radial direction. The radial direction contains both incident and scattered energy, whereas off-radial directions contain only scattered energy. The

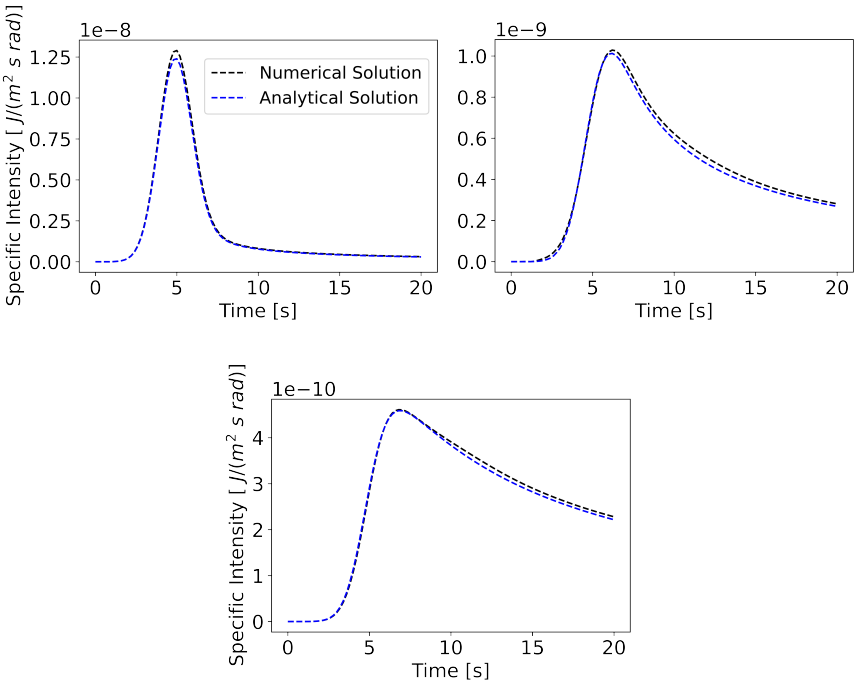

Figure 2. Comparison of analytical and numerical specific intensities at a distance of 1 scattering mean free length (5000 m) for isotropic scattering ($g = 0$). The three pannels from left to right show the specific intensities at an angle of $0, \pi/4, \pi/2$ relative to the radial direction, respectively.

scattered energy decreases in amplitude with increasing angle relative to the radial direction, as shown by Paasschens (1997). Our numerical solutions in fig. 2 agree within 3% with the exact solutions. The largest error arises near the coherent wave arrival for the specific intensity along the radial direction. This mismatch occurs because of the limited number of angular directions, and the error decreases if one uses more discretization angles. The fact that we match the exact solution well indicates that our algorithm is able to model the specific intensities, rather than just the total intensity. Therefore, the algorithm that we are showing in this paper is applicable for problems in which one wants to model the directionality of wave transport.

3.2 The spatial dependence of wave propagation

3.2.1 Isotropic scattering

As waves propagate through scattering media their wave propagation regime changes from ballistic to single scattering to multiple scattering to diffusive. To study the spatial dependence of the propagation regime we consider a numerical experiment with a Gaussian initial condition at the center of the computational domain, as in fig. 1, and isotropic scattering. The simulation parameters are the same as for fig. 2. Fig. 3 shows cross-sections of the total intensity at $y = 0$ for different simulation times. At early times ($t \ll \tau_s$) the energy is still concentrated near the source vicinity and little scattering has occurred. At later times ($t = 1\tau_s$) there is outgoing ballistic energy, with scattered energy in-between. This energy is generated by single and multiple scattering. At a later time of $t = 2\tau_s$ the scattered energy starts to dominate over the ballistic energy. This corresponds to a transfer of energy from incident to scattered waves. The scattering energy now contains single and multiple scattering energy, part of which has become diffusive. This diffusive character produces a Gaussian shape between the ballistic peaks as one expects from the solution to the diffusion equation (Sato et al., 2012). In this diffusive regime equipartitioning starts to occur, whereby the intensity wave field does not have a preferred direction of propagation. However, as we will show later, equipartitioning is necessary but not sufficient for the intensity field to be diffuse. On the panel in the lower right the scattered energy dominates, there is nearly no ballistic energy left, and the propagation becomes diffusive, as indicated by the Gaussian shape. The rapid drop at the edges of the computational domain occurs because of the vanishing boundary condition. At late times, after sufficiently many scattering events, one assumes that the wave field is equipartitioned (i.e., no preferential propagation direction) and follows a random-walk-like behaviour. However, one usually assumes that equipartitioning occurs when the condition $t \gg \tau^*$ is satisfied, rather than the condition $t \gg r/v + \tau^*$. In this

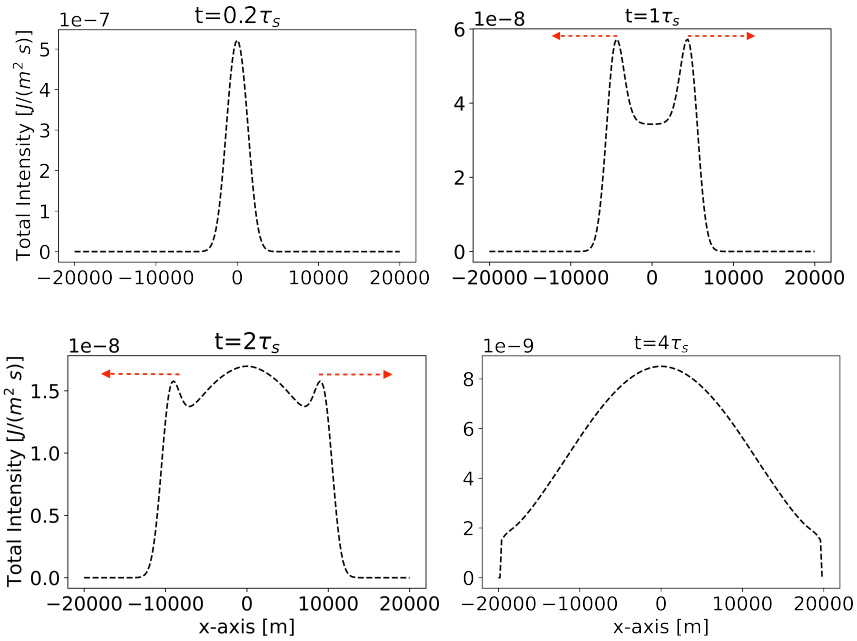

Figure 3. Cross-section of the total intensities for isotropic scattering. The red arrows indicate the outgoing ballistic energy.

expression r is the source-receiver distance, v is the speed of transport, and τ^* is the transport mean free path, which for isotropic scattering equals the scattering mean free time τ_s. The second condition is stricter because it accounts for the scattering events after the ballistic arrival.

The assumption that the field is nearly equipartitioned is typically regarded as a sufficient condition for the diffusive approximation to the scalar RTE, and it is common practice to use such approximation (Campillo, 2006; Obermann et al., 2013). However, for equipartitioning to imply diffusion, the transport mean free time times the temporal rate of change of the local current density must be much smaller than the local current density. See expression 52 and 53 in van Rossum and Nieuwenhuizen (1999) where they outline the necessary conditions to derive the diffusive approximation to radiative transfer.

To quanitify the degree of equipartitioning we introduce the *equipartitioning index*

$$\delta(\mathbf{r},t) = \frac{\sigma(\mathbf{r},t)}{\sqrt{N}\mu(\mathbf{r},t)}, \tag{15}$$

where $\sigma(\mathbf{r},t)$ is the standard deviation of the specific intensities along the angular directions defined with a division by $N-1$ as $\sigma^2(\mathbf{r},t) = \frac{1}{N-1}\sum_{i=1}^{N}(I(\mathbf{r},t,\hat{\mathbf{n}}_i) - \mu(\mathbf{r},t))^2$. $\mu(\mathbf{r},t) = \frac{1}{N}\sum_{i=1}^{N} I(\mathbf{r},t,\hat{\mathbf{n}}_i)$ is the mean of the specific intensities along the angular direction, and N is the number of angular directions. The quantity δ provides a measure of the variation of the specific intensities along the angular directions as a function of space and time. We compute the standard deviation and the mean of the specific intensities along the N propagation directions for a fixed point in space and time. The constant $1/\sqrt{N}$ is included so that $0 < \delta < 1$. Consider an uni-directional intensity field $I_i = I_0\delta_{i,1}$, where I_0 is the intensity along the only non-zero direction and $\delta_{i,j}$ is the kronecher delta. The mean for this intensity field is $\mu = I_0/N$. The standard deviation for the same intensity field is $\sigma = I_0/\sqrt{N}$, which gives $\sigma/\mu = \sqrt{N}$. The equipartitioning index is 0 when the intensity field is fully equipartitioned (i.e., same specific intensity along all directions) and 1 when the intensity field is unidirectional (i.e., all of the specific intensities but one are equal to zero).

In the first numerical experiment we release the energy within the Gaussian equally along all directions, meaning that the field is equipartitioned at $t = 0$. However, due to the nonzero gradient of the intensity field part of the intensity propagates away from the initial Gaussian with a preferred propagation direction and equipartitioning breaks down ($\delta \neq 0$) due to the directionality of the energy transport. Fig 4 shows δ for the same cross-section as fig. 3. The ballistic arrival shows the highest value of δ. Even at very early times ($t = 0.2\tau_s$) the intensity field is not equipartitioned anymore despite the initial condition being equipartitioned, as explained above. The scattering energy in between the ballistic peaks starts to equipartition over time, with the lowest δ value at $x = 0$. Even at late times the value of δ is only small (< 0.1) between -10000 and 10000 m, where more scattering events have occurred relative to those events near the ballistic arrival. One should use the condition $t \gg r/v + \tau^*$ for assessing equipartitioning

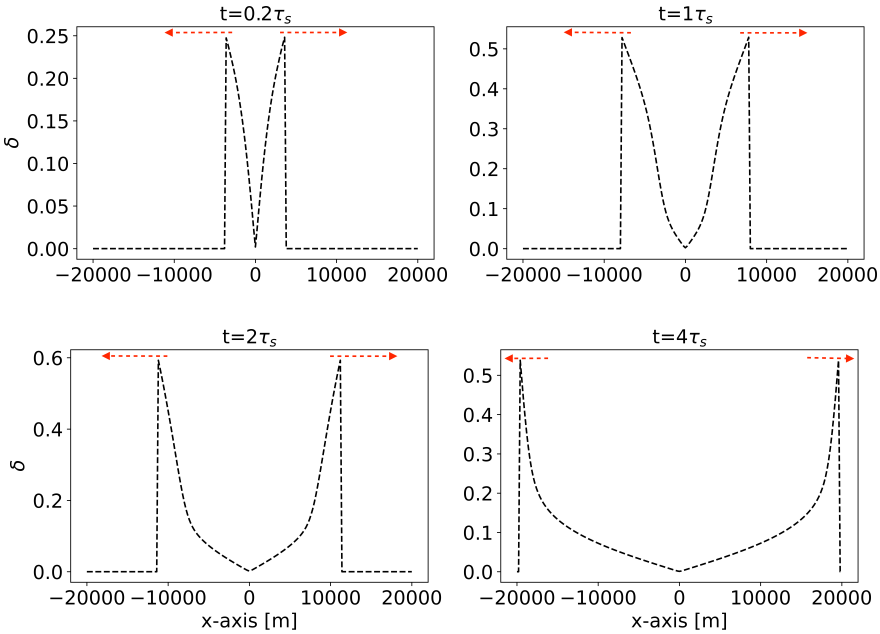

Figure 4. Cross-section of equipartitioning index δ for the isotropic source experiment. The red arrows indicate outgoing ballistic energy.

to account for multiple scattering after the ballistic arrival. To see why this condition is necessary, consider the two terms at the right hand side of the inequality. The first term r/v accounts for the travel time of the ballistic wave from the source to receiver locations. The second term, τ^*, is the transport mean free path, which is a measure of the time scale over which scattering occurs. Both of these terms together describe the time necessary for multiple scattering, and therefore equipartitioning, to develop after the ballistic wave arrival. In particular, one can not generally say that the field is equipartitioned because the level of equipartitioning depends on location.

3.2.2 Angle-dependent scattering

For realistic applications of the scalar RTE it is necessary to consider the effect of angle-dependent scattering. To this end, we study the spatial dependence of wave propagation when the scattering function depends on angular direction. Here, we investigate a medium in which forward scattering dominates. We initialize the intensities and set-up the computational domain as in the isotropic simulation to provide a just comparison between the numerical experiments.

Fig. 5 shows a cross-section along the x-axis at $y = 0$ of the total intensity for different levels of angle-dependent scattering. The scattering function is given by eqn. 12 with $g = 0, 0.3, 0.5$ for isotropic, weak, and medium forward scattering, respectively. Overall, this numerical simulation shows the same behavior as for the isotropic case. However, as forward scattering becomes stronger, it takes a longer time for the ballistic energy to become scattered. To see why this is the case consider a unidirectional intensity source. As forward scattering becomes stronger the energy of the ballistic wave takes longer to scatter due to the preferred propagation direction and the energy in-between the outgoing ballistic peaks takes a longer time to become diffusive. This behavior occurs because as forward scattering increases so does the transport mean free path, the time scale over which scattering occurs.

These numerical simulations show that our algorithm is applicable to media with angle-dependent scattering. Our results are in agreement with two physical principles. The first one is that with increasing forward scattering it takes more time for the energy to be scattered away from the ballistic wave, and the second one is that as forward scattering increases, the intensity field takes a longer time to become diffusive. As with the isotropic case there is a spatial dependence of the transition from ballistic to diffusive waves. To explore the degree of equipartitioning when scattering depends on angle we compute the equipartitioning index δ for the same cross-section as in fig. 4. Fig. 6 shows δ for this cross-section. Overall, the behavior is the same as for isotropic scattering. As before, the ballistic arrival shows the highest δ, and the lowest δ is at $x = 0$, at the center of the computational domain. For all degrees of angle-dependent scattering the equipartition index is nearly the same. This occurs because the field starts equipartitioned at $t = 0$ so that different values of g do not affect the value of δ in-between the outgoing ballistic energy.

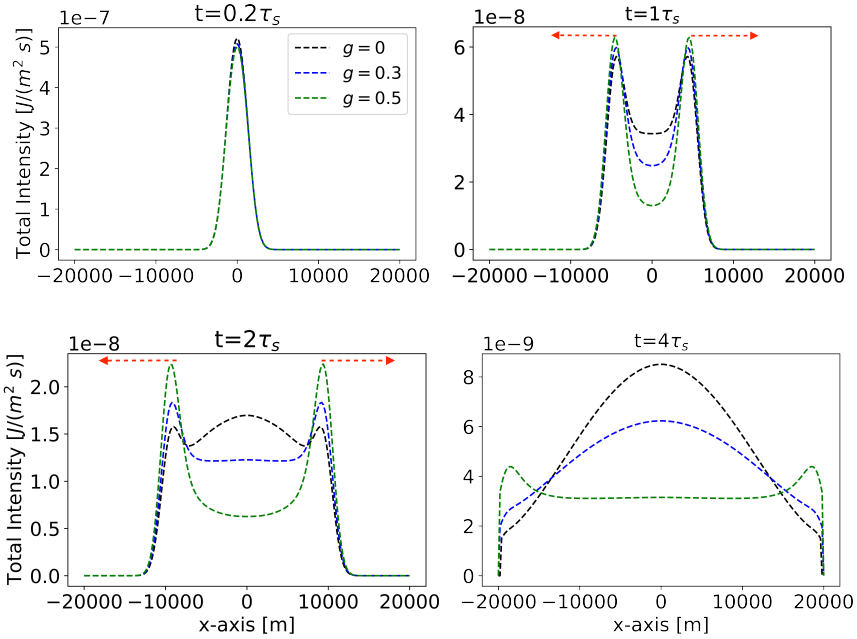

Figure 5. Cross-section of the total intensities for different levels of angle-dependent scattering and simulation times. The black, blue, and green curves correspond to $\tau^* = 1, 1.43, 2\tau_s$, respectively. The red arrows indicate the outgoing ballistic energy.

Consider the bottom left panel in fig. 6. Between -5000 and 5000 m, $\delta < 0.1$. This implies that for these distances the intensity fields are close to being equipartitioned. The bottom left panel of fig. 4 shows that for the same range only the isotropic curve is diffuse. This comparison shows that even if a field is equipartitioned it is not necessarily diffuse because equipartitioning is a necessary but not sufficient condition for the intensity to be diffuse.

van Rossum and Nieuwenhuizen (1999) derive a diffusion equation from the 3-D version of equation 1. To this end they make two assumptions. The first assumption is that the intensity distribution is almost isotropic so that the energy current $\mathbf{J}$ is much smaller than the energy density I^{tot}. With this assumption they expand the specific intensities as

$$I(\mathbf{r}, \hat{\mathbf{n}}, t) \approx I^{\text{tot}}(\mathbf{r}, t) + 3v\hat{\mathbf{n}} \cdot \mathbf{J}(\mathbf{r}, t), \tag{16}$$

where they ignore the higher order terms since these terms become negligible. The variables I^{tot} and $\mathbf{J}$ are the local radiation and current densities, respectively. They then assume that the intensity field satisfies

$$\left|\tau^* \partial_t \mathbf{J}\right| \ll \left|\mathbf{J}\right|, \tag{17}$$

with which they obtain the diffusive approximation to the scalar RTE.

To estimate the necessary condition for diffusion we rewrite the condition 17 as

$$\epsilon = \left|\frac{\tau^* \partial_t I^{\text{tot}}}{I^{\text{tot}}}\right| \ll 1, \tag{18}$$

where we have replaced the local current density $\mathbf{J}$ by the local radiation density I^{tot}.

Recall that in fig. 5 the diffuse character of the scattered waves only starts to appear at a time $t = 2\tau_s$. Fig. 7 shows ϵ from equation 18 for the bottom left and right panels, respectively, of fig. 5, with the x-axis now ranging from -6000 to 6000 m to focus on the diffuse character of the scattered waves. The left panel of fig. 7 shows the lowest value of ϵ for isotropic scattering, and it increases as forward scattering becomes stronger. This reflects that energy that scatters isotropically reaches a diffuse state more rapidly than when forward scattering dominates, as we showed in fig. 5. The left panel of fig. 7 also shows that, as with equipartitioning, ϵ changes locally. The smallest value of ϵ is near $x = 0$ and increases away from this location. This local behavior is more evident with stronger forward scattering ($g = 0.5$). The right panel of fig. 7 also shows higher ϵ for stronger forward scattering. It also shows that ϵ decreases with time because the scattered waves start to become diffuse. As before, this diffuse behavior changes locally, but with less variations than for earlier times.

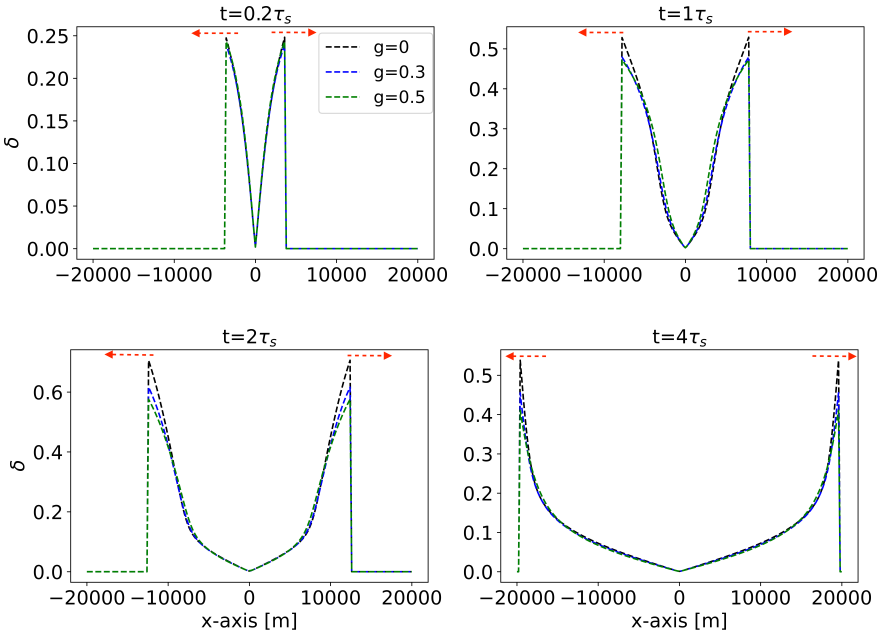

Figure 6. Cross-section of equipartitioning index δ for the isotropic source experiment. The red arrows indicate outgoing ballistic energy.

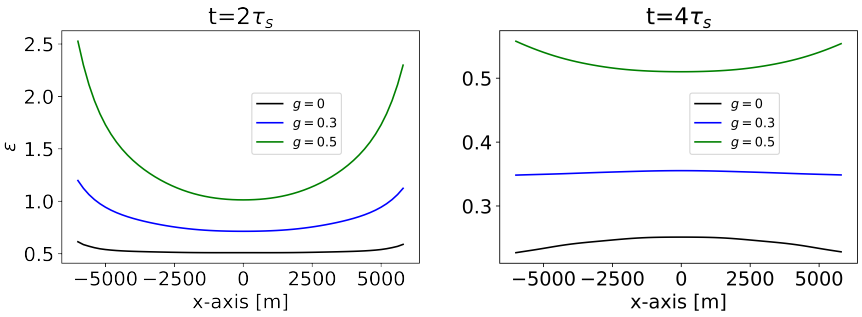

Figure 7. Diffusion condition 18 for the bottom left and bottom right panels in fig. 5, with the x-axis now ranging from -6000 to 6000 m.

3.2.3 Directional source and angle-dependent scattering

So far we have explored the spatial dependence on wave propagation due to the scattering properties of the medium. We extend our numerical study by considering a segement of a plane-wave which propagates from left to right. As before, we test for isotropic, weak forward, and medium forward scattering ($g = 0.0, 0.3, 0.5$), which correspond to transport mean free times $\tau^* = 1, 1.43, 2\tau_s$, respectively. Fig. 8 shows the initial condition and computational domain for this numerical test. We place the plane wave segment around the origin with the x-coordinate ranging from -20000 to 20000 m and the y-coordinate ranging from -20000 to 20000 m. The only non-zero specific intensity at time $t = 0$ corresponds to $\theta = 0$. We taper the plane-wave segment along both horizontal (-1000 to 1000 m) and vertical (-2500 to 2500 m) directions so that the numerical interpolation is accurate. Fig. 9 shows a cross-section at the middle of the computational domain along the x-axis for the plane wave segment simulation. As with the isotropic initial condition, when time progresses the intensity with stronger forward scattering has more energy concentrated along the ballistic arrival and less trailing scattered energy. A secondary "ballistic" wave, caused by waves that are backscattered immediately after the plane wave segment is launched, is indicated by the orange arrow and propagates towards the left of the computational domain. This secondary arrival has a negligible amplitude. Fig. 10 shows the equipartitioning index δ for the intensity cross-section in Fig. 9. The ballistic arrival shows the highest equipartitioning indexδ, as in the previous simulations. The secondary "ballistic" arirval that arises early in the simulation shows up as a secondary peak on the left side of fig. 10, but the intensity corresponding to this peak is negligible. The scattering energy directly behind the peak propagating to the right shows the lowest δ. The directionality

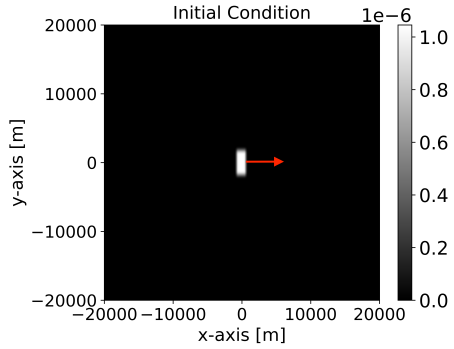

Figure 8. Normalized initial condition for the specific intensity of a plane-wave segment aligned with the positive x-axis, all other specific intensities are set equal to zero. The red arrow indicates the initial direction of wave propagation.

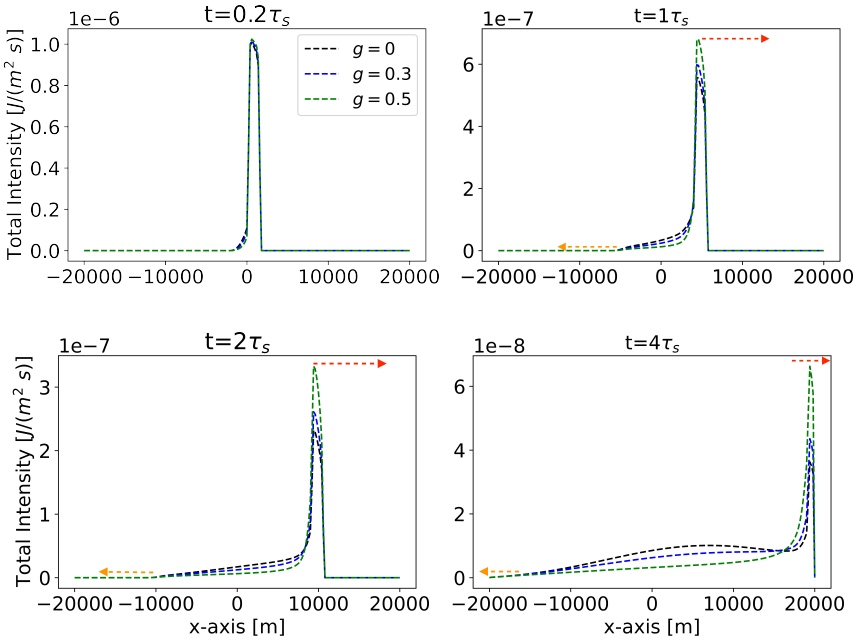

Figure 9. Cross-section of the total intensities for different levels of angle-dependent scattering and simulation times. The black, blue, and green curves correspond to $\tau^* = 1, 1.43, 2\tau_s$, respectively. The red arrow indicates the right-going ballistic wave, the orange arrow indicates a secondary "ballistic" arrival which arises due to backscattering.

in wave propagation occurs because the initial condition has a preferred propagation direction. For this type of initial condition one should also use the condition $t \gg r/v + \tau^*$ to account for both the primary ballistic arrival (propagating from left to right) and the secondary wave (propagating to the left). Fig. 10 also shows scattered energy with higher δ as forward scattering increases, which is most prominent at later times. This occurs because for this numerical test the initial condition has a preferred propagation direction so that g plays a role in determining equipartitioning.

3.3 Non-uniform scattering

To extend the capability of our algorithm we consider media with non-uniform scattering mean free time, while keeping the speed of transport constant. This scenario corresponds to a scatterer density that depends on location in a background medium of constant

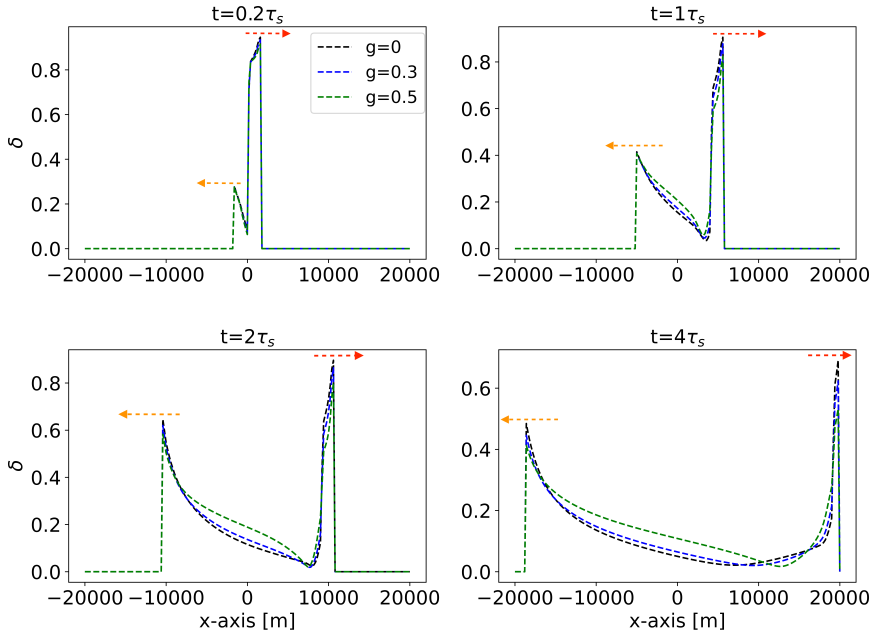

Figure 10. Cross-section of equipartitioning index δ for the plane source experiment. The red arrow indicates the right-going ballistic wave, the orange arrow indicates a secondary "ballistic" arrival which arises due to backscattering.

velocity. When the scattering mean free time varies non-uniformly over space we replace the integral equation 5 by

$$I(\mathbf{r},\hat{\mathbf{n}},t) = I(\mathbf{r}-v(t-t_0)\hat{\mathbf{n}},\hat{\mathbf{n}},t_0)exp\Big(-\int_{l_c}\frac{1}{v\tau_s(s')}ds'\Big)$$
$$+\int_{t_0}^{t}\frac{1}{\tau_s(\mathbf{r}-v(t-t')\hat{\mathbf{n}})}\oint f(\hat{\mathbf{n}},\hat{\mathbf{n}}')I(\mathbf{r}-v(t-t')\hat{\mathbf{n}},\hat{\mathbf{n}}',t')exp\Big(-\int_{l_d}\frac{1}{v\tau_s(s')}ds'\Big)d^2\hat{\mathbf{n}}'dt', \tag{19}$$

where l_c is the direct path from $\mathbf{r}-v(t-t_0)\hat{\mathbf{n}}$ to $\mathbf{r}$ and l_d is the direct path from $\mathbf{r}-v(t-t')\hat{\mathbf{n}}$ to $\mathbf{r}$. The approach to show that the integral equation 19 satisfies the radiative transfer equations 3 is similar to the one shown in the appendix. The rest of the formulation follows the procedure outlined in section 2. To compute the integral appearing in the exponential we use a weighted average between neighboring points.

We show numerical experiments for two different media with isotropic scattering: A medium with constant scattering mean free time $\tau_s = 5$ s, and a medium which consists of three layers where the first and third layer have a scattering mean free time of 5 s while the middle layer has a scattering mean free time of 2.5 s. Fig. 11 shows the layered medium in the corresponding computational domain. We initialize the intensities with a plane wave segment that propagates upward. Fig. 12 shows this initial condition along with the computational domain that we use. The x-axis now ranges from -10000 to 10000 m, the temporal, spatial and angular sampling is the same as in the previous section. We taper the plane wave from -2500 to 2500 m in the horizontal direction and -9000 to -7000 m in the vertical direction. Fig. 13 shows cross-sections of the total intensity along the y-axis at $x = 0$ for media with variable and constant scattering mean free time. At early times ($t = 2$ s), before the waves reach the boundary at $y = -5000$ m, the total intensities are the same since the ballistic peak has not sampled the variation in scattering properties. At intermediate times ($t = 5$ s and $t = 7$ s) the ballistic peak and the scattered energy for the total intensity with variable scattering becomes less than that for constant scattering. This occurs because the effective scattering mean free time for the intensity with variable scattering is less than that for constant scattering. At late times ($t = 10$ s) the intensity for variable scattering is much lower than that with constant scattering since the wave spends most of its propagation time in a medium with a scattering mean free time which is half of the one for constant scattering.

4 IMPLICATIONS FOR GREEN'S FUNCTION RECONSTRUCTION

Weaver and Lobkis (2001) proposed to reconstruct Green's functions in an ultrasonic experiment using thermal field fluctuations,

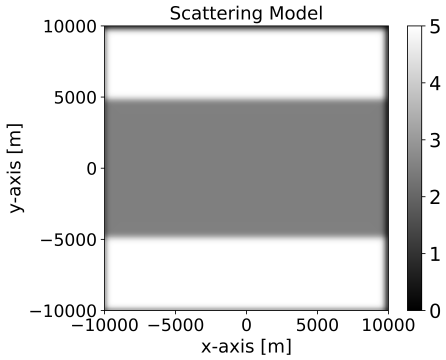

Figure 11. Scattering model that we use in the experiments for non-uniform scattering media. The grey scale bar shows the scattering mean free time in seconds.

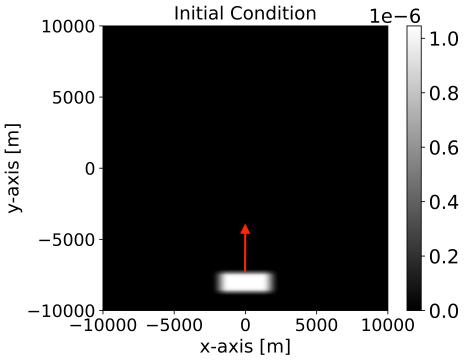

Figure 12. Initial condition of an upward propagating plane wave segment. The red arrow indicates the initial direction of wave propagation.

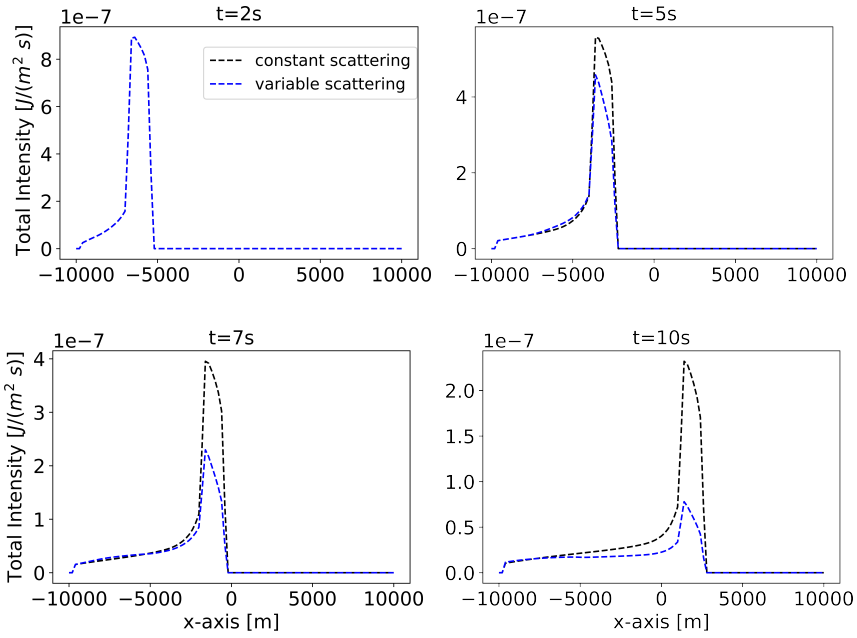

Figure 13. Total intensity along the y-axis at $x = 0$ for different times.

assuming that such field is equipartitioned. In the field of acoustics and seismology, this work inspired the development of *seismic interferometry* (Curtis et al., 2006; Roux et al., 2005; Snieder and Larose, 2013). In this technique one retrieves the causal and anti-causal Green's functions between receiver locations A and B, by cross-correlating the wave fields recorded at such locations due to an even distribution of sources, assuming that the wave field has no preferred propagation direction (equipartitioning). Snieder et al. (2010) showed that equipartitioning is necessary for Green's function retrieval but not sufficient.

In practice this equipartitioning assumption does not always hold. Paul et al. (2005) computed field-field correlations of Alaskan earthquakes to retrieve the causal and anti-causal Green's functions. In theory, if the noise wave field were equipartitioned, these Green's functions should be symmetric in time. However, they found that the correlations they computed were asymmetric in time, which they suggest is due to the preferred direction of energy flow of the coda waves that they use to compute the field-field correlations. When they use late coda they find that this asymmetry remains, but to a lesser extent than when using earlier coda. Stehly et al. (2006) showed that the noise, which one may use to reconstruct Green's functions near coastlines, radiates preferentially away from storms at the oceans. This preferential directionality of the noise radiation affects the asymmetry of the Green's function that one retrieves, especially if the noise field that one uses is uni-directional and not evenly distributed.

5 DISCUSSION

The numerical algorithm that we propose to solve the scalar RTE in a medium with uniform speed of transport, non-uniform scattering mean free time, and arbitrary angle-dependent scattering allows us to compute the specific intensities, as opposed to just the total intensities. This algorithm can be used in applications where one needs to resolve the angular distribution of the wave energy transport. We can use our algorithm for an intensity with a sufficiently smooth initial condition (i.e., enough sampling points in space so that the interpolation does not introduce numerical artifacts), as we showed through numerical experiments with isotropic and plane wave segment initial conditions in a medium with angle-dependent scattering and varying scattering properties (Fig. 5, 9, and 13). In our algorithm we discretize the angular integral and then handle the advection of energy analytically so that we do not introduce the dispersion errors appearing in numerical techniques such as finite differences or discontinuous Galerkin finite element methods. This numerical dispersion may cause negative intensities which are non-physical. Due to the limited number of angular directions in the discrete ordinate method, our algorithm introduces a small error around the ballistic arrival. Fig. 2 shows that this error does not affect the accuracy of the numerical scattered specific intensities, and one may reduce such error by increasing the number of discretization angles. Since we compute the specific intensities, our algorithm is useful for testing and understanding the equipartitioning of an intensity field. We quantify the extent of randomization of an intensity field through the equipartitioning index. We find that, in general, the level of equipartitioning of an intensity field is a function of space and time. Figs. 6 and 10 show that the ballistic arrival has the highest equipartitioning index and that the trailing scattered energy becomes equipartitioned over time but not at the same rate throughout the computational domain. The difference in the rate at which equipartitioning occurs requires one to use the condition $t \gg r/v + \tau^*$ as a measure of equipartitioning to account for the scattering events following the ballistic arrival. This condition indicates that the wave propagation regime varies spatially. Comparison of Figs. 6 and 10 shows that for assessing equipartitioning one needs to consider the initial condition of the intensity field. In the plane wave segment simulation the energy directly behind the right-going peak quickly randomizes, but as one moves closer to the secondary "ballistic" wave (left-going) the wave field has a preferred propagation direction due to backscattering early in the simulation. This again indicates that the wave propagation regime depends on space. We also showed numerically that even though equipartitioning is necessary, it is not sufficient for an intensity field to be diffuse. This is because the diffusive approximation requires the temporal derivative of the energy flux to be small, as condition 17 shows. This condition implies that one must distiniguish between equipartitioning and diffusion. Local equipartitioning has implications for Green's functions retrieval. One particular example is *seismic interferometry* where the extent of equipartitioning affects the accuracy of the Green's functions that one recovers. Since equipartitioning changes locally rather than globally, the accuracy of the Green's function reconstruction may depend on space and time.

6 ACKNOWLEDGEMENTS

We thank the sponsor companies of the Center for Wave Phenomena, whose support made this research possible.

REFERENCES

Abdoulaev, G. S., 2003, Three-dimensional optical tomography with the equation of radiative transfer: Journal of Electronic Imaging, **12**, 594–601.

Aumann, H. H., X. Chen, E. Fishbein, A. Geer, S. Havemann, X. Huang, X. Liu, G. Liuzzi, S. DeSouza-Machado, E. M. Manning, G. Masiello, M. Matricardi, I. Moradi, V. Natraj, C. Serio, L. Strow, J. Vidot, R. Chris Wilson, W. Wu, Q. Yang, and Y. L. Yung, 2018, Evaluation of Radiative Transfer Models With Clouds: Journal of Geophysical Research: Atmospheres, **123**, 6142–6157.

Baes, M., and H. Dejonghe, 2001, Radiative transfer in disc galaxies - I. A comparison of four methods to solve the transfer equation in plane-parallel geometry: Monthly Notices of the Royal Astronomical Society, **326**, 722–732.

Campillo, M., 2006, Phase and Correlation in 'Random' Seismic Fields and the Reconstruction of the Green Function: Pure and Applied Geophysics, **163**, 475–502.

Camps, P., and M. Baes, 2018, The Failure of Monte Carlo Radiative Transfer at Medium to High Optical Depths: The Astrophysical Journal, **861**, 80.

Chandrasekhar, S., 1960, Radiative transfer: Dover Publications.

Clarke, P., H. Wang, J. Garrard, R. Abedi, and S. Mudaliar, 2019, Space-angle discontinuous Galerkin method for plane-parallel radiative transfer equation: Journal of Quantitative Spectroscopy and Radiative Transfer, **233**, 87–98.

Curtis, A., P. Gerstoft, H. Sato, R. Snieder, and K. Wapenaar, 2006, Seismic interferometry—turning noise into signal: The Leading Edge, **25**, 1082–1092.

de Abreu, M. P., 2004, A two-component method for solving multislab problems in radiative transfer: Journal of Quantitative Spectroscopy and Radiative Transfer, **85**, 311–336.

Dinther, C., L. Margerin, and M. Campillo, 2021, Implications of Laterally Varying Scattering Properties for Subsurface Monitoring With Coda Wave Sensitivity Kernels: Application to Volcanic and Fault Zone Setting: Journal of Geophysical Research: Solid Earth, **126**.

Duran, A., T. Planès, and A. Obermann, 2020, Coda-wave decorrelation sensitivity kernels in 2-D elastic media: a numerical approach: Geophysical Journal International, **223**, 934–943.

Evans, K. F., and G. L. Stephens, 1995, Microwave Radiative Transfer through Clouds Composed of Realistically Shaped Ice Crystals. Part II. Remote Sensing of Ice Clouds: Journal of the Atmospheric Sciences, **52**, 2058–2072.

Fan, Y., J. An, and L. Ying, 2019, Fast algorithms for integral formulations of steady-state radiative transfer equation: Journal of Computational Physics, **380**, 191–211.

Francis, P. N., M. C. Cooke, and R. W. Saunders, 2012, Retrieval of physical properties of volcanic ash using Meteosat: A case study from the 2010 Eyjafjallajökull eruption: Meteosat Volcanic Ash Retrievals: Journal of Geophysical Research: Atmospheres, **117**.

Han, W., J. Huang, and J. A. Eichholz, 2010, Discrete-Ordinate Discontinuous Galerkin Methods for Solving the Radiative Transfer Equation: SIAM Journal on Scientific Computing, **32**, 477–497.

Hofmeister, A., 2005, Dependence of diffusive radiative transfer on grain-size, temperature, and Fe-content: Implications for mantle processes: Journal of Geodynamics, **40**, 51–72.

Iwabuchi, H., 2006, Efficient Monte Carlo Methods for Radiative Transfer Modeling: Journal of the Atmospheric Sciences, **63**, 2324–2339.

Kanu, C., and R. Snieder, 2015, Numerical computation of the sensitivity kernel for monitoring weak changes with multiply scattered acoustic waves: Geophysical Journal International, **203**, 1923–1936.

Klose, A. D., and A. H. Hielscher, 1999, Iterative reconstruction scheme for optical tomography based on the equation of radiative transfer: Medical Physics, **26**, 1698–1707.

Klose, A. D., U. Netz, J. Beuthan, and A. H. Hielscher, 2002, Optical tomography using the time-independent equation of radiative transfer — Part 1: forward model: Journal of Quantitative Spectroscopy and Radiative Transfer, **72**, 691–713.

Le Hardy, D., Y. Favennec, and B. Rousseau, 2016, Solution of the 2-D steady-state radiative transfer equation in participating media with specular reflections using SUPG and DG finite elements: Journal of Quantitative Spectroscopy and Radiative Transfer, **179**, 149–164.

Lee, K. H., M. S. Wong, S.-R. Chung, and E. Sohn, 2014, Improved volcanic ash detection based on a hybrid reverse absorption technique: Atmospheric Research, **143**, 31–42.

Manners, J., J.-C. Thelen, J. Petch, P. Hill, and J. Edwards, 2009, Two fast radiative transfer methods to improve the temporal sampling of clouds in numerical weather prediction and climate models: Fast Rt Methods For Temporal Sampling of Clouds: Quarterly Journal of the Royal Meteorological Society, **135**, 457–468.

Margerin, L., T. Planès, J. Mayor, and M. Calvet, 2016, Sensitivity kernels for coda-wave interferometry and scattering

tomography: theory and numerical evaluation in two-dimensional anisotropically scattering media: Geophysical Journal International, **204**, 650–666.

Narayanan, D., M. J. Turk, T. Robitaille, A. J. Kelly, B. C. McClellan, R. S. Sharma, P. Garg, M. Abruzzo, E. Choi, C. Conroy, B. D. Johnson, B. Kimock, Q. Li, C. C. Lovell, S. Lower, G. C. Privon, J. Roberts, S. Sethuram, G. F. Snyder, R. Thompson, and J. H. Wise, 2021, Powderday: Dust Radiative Transfer for Galaxy Simulations: The Astrophysical Journal Supplement Series, **252**, 12.

Noebauer, U. M., and S. A. Sim, 2019, Monte Carlo radiative transfer: Living Reviews in Computational Astrophysics, **5**, 1.

Obermann, A., T. Planès, C. Hadziioannou, and M. Campillo, 2016, Lapse-time-dependent coda-wave depth sensitivity to local velocity perturbations in 3-D heterogeneous elastic media: Geophysical Journal International, **207**, 59–66.

Obermann, A., T. Planès, E. Larose, C. Sens-Schönfelder, and M. Campillo, 2013, Depth sensitivity of seismic coda waves to velocity perturbations in an elastic heterogeneous medium: Geophysical Journal International, **194**, 372–382.

Ostashev, V. E., M. B. Muhlestein, and D. K. Wilson, 2017, Radiative transfer formulation for forest acoustics: The Journal of the Acoustical Society of America, **142**, 3767–3780.

Paasschens, J. C. J., 1997, Solution of the time-dependent Boltzmann equation: Physical Review E, **56**, 1135–1141.

Paul, A., M. Campillo, L. Margerin, E. Larose, and A. Derode, 2005, Empirical synthesis of time-asymmetrical Green functions from the correlation of coda waves: Journal of Geophysical Research, **110**, B08302.

Planès, T., E. Larose, L. Margerin, V. Rossetto, and C. Sens-Schönfelder, 2014, Decorrelation and phase-shift of coda waves induced by local changes: multiple scattering approach and numerical validation: Waves in Random and Complex Media, **24**, 99–125.

Prata, A. J., 1989, Infrared radiative transfer calculations for volcanic ash clouds: Geophysical Research Letters, **16**, 1293–1296.

Przybilla, J., and M. Korn, 2008, Monte Carlo simulation of radiative energy transfer in continuous elastic random media-three-component envelopes and numerical validation: Geophysical Journal International, **173**, 566–576.

Przybilla, J., M. Korn, and U. Wegler, 2006, Radiative transfer of elastic waves versus finite difference simulations in two-dimensional random media: Journal of Geophysical Research, **111**, B04305.

Quijano, J. E., and L. M. Zurk, 2009, Radiative transfer theory applied to ocean bottom modeling: The Journal of the Acoustical Society of America, **126**, 1711.

Reboul, E., A. Le Bot, and J. Perret-Liaudet, 2005, Radiative transfer equation for multiple diffraction: The Journal of the Acoustical Society of America, **118**, 1326–1334.

Ren, K., G. S. Abdoulaev, G. Bal, and A. H. Hielscher, 2004, Algorithm for solving the equation of radiative transfer in the frequency domain: Optics Letters, **29**, 578.

Roberge, W. G., 1983, The spherical harmonics solution for the radiation field in plane-parallel clouds with embedded sources: The Astrophysical Journal, **275**, 292.

Rossetto, V., L. Margerin, T. Planès, and r. Larose, 2011, Locating a weak change using diffuse waves: Theoretical approach and inversion procedure: Journal of Applied Physics, **109**, 034903.

Roux, P., K. G. Sabra, W. A. Kuperman, and A. Roux, 2005, Ambient noise cross correlation in free space: Theoretical approach: The Journal of the Acoustical Society of America, **117**, 79–84.

Ryzhik, L., G. Papanicolaou, and J. B. Keller, 1996, Transport equations for elastic and other waves in random media: Wave Motion, **24**, 327–370.

Sato, H., M. C. Fehler, and T. Maeda, 2012, Seismic Wave Propagation and Scattering in the Heterogeneous Earth : Second Edition: Springer Berlin Heidelberg.

Snieder, R., A. Duran, and A. Obermann, 2019, Locating velocity changes in elastic media with coda wave interferometry, *in* Seismic ambient noise: Cambridge University Press, 188–217. (Section: 6).

Snieder, R., Y. Fan, E. Slob, and K. Wapenaar, 2010, Equipartitioning is not sufficient for Green's function extraction: Earthquake Science, **23**, 403–415.

Snieder, R., and E. Larose, 2013, Extracting Earth's Elastic Wave Response from Noise Measurements: Annual Review of Earth and Planetary Sciences, **41**, 183–206.

Stehly, L., M. Campillo, and N. M. Shapiro, 2006, A study of the seismic noise from its long-range correlation properties: Journal of Geophysical Research, **111**, B10306.

Steinacker, J., A. Bacmann, and T. Henning, 2002, Application of adaptive multi-frequency grids to three-dimensional astrophysical radiative transfer: Journal of Quantitative Spectroscopy and Radiative Transfer, **75**, 765–786.

Turner, J. A., and R. L. Weaver, 1994, Radiative transfer of ultrasound: The Journal of the Acoustical Society of America, **96**, 3654–3674.

van Rossum, M. C. W., and T. M. Nieuwenhuizen, 1999, Multiple scattering of classical waves: microscopy, mesoscopy, and diffusion: Reviews of Modern Physics, **71**, 313–371.

Weaver, R. L., and O. I. Lobkis, 2001, Ultrasonics without a Source: Thermal Fluctuation Correlations at MHz Frequencies: Physical Review Letters, **87**, 134301.

Wolf, S., 2003, Efficient Radiative Transfer in Dust Grain Mixtures: The Astrophysical Journal, **582**, 859–868.

Wu, R.-S., 1985, Multiple scattering and energy transfer of seismic waves – separation of scattering effect from intrinsic attenuation – I. Theoretical modelling: Geophysical Journal International, **82**, 57–80.

Xu, F., A. B. Davis, R. A. West, J. V. Martonchik, and D. J. Diner, 2011, Markov chain formalism for vector radiative transfer in a plane-parallel atmosphere overlying a polarizing surface: Optics Letters, **36**, 2083.

Yodh, A., and B. Chance, 1995, Spectroscopy and Imaging with Diffusing Light: Physics Today, **48**, 34–40.

Yoshimoto, K., 2000, Monte Carlo simulation of seismogram envelopes in scattering media: Journal of Geophysical Research: Solid Earth, **105**, 6153–6161.

Appendix: Integral equation 5 as a solution to the radiative transfer equations 3

We show that the integral equation 5 satisfies the radiative transfer equations 3 with the initial condition 4. Inserting $t = t_0$ in equation 5 gives the initial condition 4. To simplify the proof we align the x-axis with $\hat{\mathbf{n}}$ so that the integral equation 5 becomes

$$\begin{aligned} I(x, y=0, \hat{\mathbf{n}}, t) &= I(x - v(t-t_0), y=0, \hat{\mathbf{n}}, t_0) e^{-(t-t_0)/\tau_s} \\ &+ \frac{1}{\tau_s} \int_{t_0}^{t} \oint f(\hat{\mathbf{n}}, \hat{\mathbf{n}}') I(x - v(t-t'), y=0, \hat{\mathbf{n}}', t') e^{-(t-t')/\tau_s} d^2\hat{\mathbf{n}}' dt', \end{aligned} \tag{20}$$

and the radiative transfer equations 3 become

$$\partial_t I(x, y=0, \hat{\mathbf{n}}, t) + v\partial_x I(x, y=0, \hat{\mathbf{n}}, t) = -I(x, y=0, \hat{\mathbf{n}}, t)/\tau_s + \oint f(\hat{\mathbf{n}}, \hat{\mathbf{n}}') I(x, y=0, \hat{\mathbf{n}}', t) d^2\hat{\mathbf{n}}'/\tau_s, \tag{21}$$

for $t > t_0$. Next, we take the derivative of equation 20 with respect to t

$$\begin{aligned} \partial_t I(x, y=0, \hat{\mathbf{n}}, t) = &- v\partial_x I\big(x - v(t-t_0), y=0, \hat{\mathbf{n}}, t_0\big) e^{-(t-t_0)/\tau_s} \\ &- \frac{1}{\tau_s} I\big(x - v(t-t_0), y=0, \hat{\mathbf{n}}, t_0\big) e^{-(t-t_0)/\tau_s} \\ &+ \frac{1}{\tau_s} \oint f(\hat{\mathbf{n}}, \hat{\mathbf{n}}') I\big(x, y=0, \hat{\mathbf{n}}', t\big) d^2\hat{\mathbf{n}}' \\ &\frac{1}{\tau_s} \int_{t_0}^{t} \oint f(\hat{\mathbf{n}}, \hat{\mathbf{n}}') \Big(- v\partial_x I\big(x - v(t-t'), y=0, \hat{\mathbf{n}}', t'\big) \Big) e^{-(t-t')/\tau_s} d^2\hat{\mathbf{n}}' dt' \\ &- \frac{1}{\tau_s^2} \int_{t_0}^{t} \oint f(\hat{\mathbf{n}}, \hat{\mathbf{n}}') I\big(x - v(t-t'), y=0, \hat{\mathbf{n}}', t'\big) e^{-(t-t')/\tau_s} d^2\hat{\mathbf{n}}' dt', \end{aligned} \tag{22}$$

and the derivative with respect to x

$$\begin{aligned} \partial_x I(x, y, \hat{\mathbf{n}}, t) &= \partial_x I\big(x - v(t-t_0), y=0, \hat{\mathbf{n}}, t_0\big) e^{-(t-t_0)/\tau_s} \\ &+ \frac{1}{\tau_s} \int_{t_0}^{t} \oint f(\hat{\mathbf{n}}, \hat{\mathbf{n}}') \partial_x I\big(x - v(t-t'), y=0, \hat{\mathbf{n}}', t'\big) e^{-(t-t')/\tau_s} d^2\hat{\mathbf{n}}' dt'. \end{aligned} \tag{23}$$

Inserting equations 22 and 23 into the radiative transfer equations 21 gives

$$\begin{aligned} \frac{\partial I(x, y=0, \hat{\mathbf{n}}, t)}{\partial t} + v\partial_x I(x, y=0, \hat{\mathbf{n}}, t) = &- \frac{1}{\tau_s} \Big(I(x - v(t-t_0), y=0, \hat{\mathbf{n}}, t_0) e^{-(t-t_0)/\tau_s} \\ &+ \frac{1}{\tau_s} \int_{t_0}^{t} \oint f(\hat{\mathbf{n}}, \hat{\mathbf{n}}') I(x - v(t-t'), y=0, \hat{\mathbf{n}}', t') e^{-(t-t')/\tau_s} d^2\hat{\mathbf{n}}' dt' \Big) \\ &+ \frac{1}{\tau_s} \oint f(\hat{\mathbf{n}}, \hat{\mathbf{n}}') I\big(x, y=0, \hat{\mathbf{n}}', t\big) d^2\hat{\mathbf{n}}'. \end{aligned} \tag{24}$$

We note that the first and second terms on the right-hand side of equation 24 correspond to the right-hand side of the integral equation 20 times τ_s^{-1}. Equation 24 then becomes

$$\frac{\partial I(x, y=0, \hat{\mathbf{n}}, t)}{\partial t} + v\partial_x I(x, y=0, \hat{\mathbf{n}}, t) = -\frac{1}{\tau_s} I\big(x, y=0, \hat{\mathbf{n}}, t\big) + \frac{1}{\tau_s} \oint f(\hat{\mathbf{n}}, \hat{\mathbf{n}}') I\big(x, y=0, \hat{\mathbf{n}}', t\big) d^2\hat{\mathbf{n}}', \tag{25}$$

which generalizes to the radiative transfer equations 3 since the orientation of the x-axis is arbitrary.